3857

Performance Analysis of a Propeller with Surface Protrusions

Yuchao Song,[1] Hongliang Yu,[2] Chih-Cheng Chen,[3,4*]
Chun-You Liu,[3] Yanxin Yang,[1] and Changkuan Chi[1]

[1]Marine Engineering College, Dalian Maritime University, 1 Linghai Road, Dalian 116026, China
[2]Marine Engineering College, Jimei University, 185 Yinjiang Road, Jimei District, Xiamen 361021, China
[3]Department of Automatic Control Engineering, Feng Chia University, Taichung 40724, Taiwan
[4]Department of Aeronautical Engineering, Chaoyang University of Technology, Taichung 413, Taiwan

For efficiency improvement and state monitoring of the propeller of a ship, a non-smooth surface is a conventional approach to reducing drag, saving energy, and providing a stabler sensing condition. In this paper, we studied the effects of the surface roughness and protrusions on propeller performance, and the hydrodynamic performance of a marine propeller, including the propeller thrust, torque, and open water efficiency, was analyzed for different surface conditions. By ANSYS meshing, the Y+ value of the rotating propeller was ensured to be less than 5. The shear stress transport (SST) turbulence model, stationary domain, and rotating domain were adopted to model the water flow during simulation in an ANSYS software CFX module. In our numerical calculations, there were four surface conditions for the rotating blade of the propeller: a non-slip smooth surface, a surface with a roughness of 5 μm, and surfaces with protrusions of 0.2 and 0.3 mm. The results show that the efficiency of the propeller is increased by protrusions located on the pressure surface. The propeller with 0.2 mm protrusions shows the best performance. Compared with the non-slip smooth wall condition, the thrust force is increased, and the increase in propeller efficiency is 2.83% when the advance coefficient of the propeller J is 0.9 and 6.40% when J is 1.0. The propeller efficiency is reduced by blade surface roughness, but the flow field is more stationary for the propeller with surface protrusions, which is beneficial for propeller shaft sensors. The other hydrodynamic parameters are also analyzed to illustrate their effect on the propeller performance.

1. Introduction

During ship maneuvering, a thrust force is imposed on the ship structure through the thrust bearing by a propeller. The propeller is an important part of the marine propulsion system. It plays a major role in the control of the ship and affects the sensing and detection system attached on its shaft. Toward saving energy, reducing carbon emission, and ensuring the effectiveness of sensors, researchers have designed new propellers with improved efficiency. Usually, the optimization of the blade section profile and the condition of the blade surface is an important technique, because the performance of a propeller is affected by fouling and cavitation.

In propeller hydrodynamic analysis, a vortex lattice method has been proposed to design propeller blade sections with an efficiency improvement of 1.2%.[1] Cavitation is also markedly suppressed by optimization of the blade section.[2] Bio-fouling roughens the smooth surface and reduces the efficiency by 11.9% when the advance coefficient of the propeller J is 0.6.[3] Non-smooth structures can reduce frictional drag. Numerical simulation results for a non-smooth surface show that an ovoid surface has a drag reduction effect; for example, it reduces the drag force by 10% when the flow velocity is 24 m/s.[4] The characteristic surface of a centrifugal pump's impeller has been used as a reference to optimize the propeller performance. The bionic dimples on the impeller deaden the large vortex, reduce the drag force, and lower the torque of the impeller caused by viscous resistance. The non-smooth surface ensures the flow of fluid near the boundary layer of the blade and reduces the wall shear stress. The concave surface of blades decreases the energy dissipation caused by turbulence, increases the stability of the internal fluid flow, and improves the efficiency of the centrifugal pump.[5]

In addition to the test method and mathematical analysis, a numerical computational fluid dynamics (CFD) method is used to model hydrodynamic behaviors in propeller hydrodynamics. Its computation cost is much lower than that of the test method, and it is suitable for use by a designer to optimize the propeller. Many researchers have used CFD as a tool in marine design, and CFD is very convenient for providing detailed characteristics in a short time. Numerical codes used in CFD include CFX, FLUENT, and STAR CCM+ software.[7–11]

In this paper, the protrusions on a pressure surface (PS) were designed to improve the propeller performance and provide a stabler condition for shaft detection and sensing systems. The numerical results are compared with those for the original propeller with a smooth surface and for the new propeller with surface roughness. Model grids are obtained by ANSYS meshing with a Y+ value less than 5. All the 3D flow models are computed by ANSYS CFX and based on the shear stress transport (SST) turbulence model.

2.   Geometric Configuration of Propeller

A four-blade propeller is designed on the basis of the blade sections and main parameters. Some parameters of this propeller and some abbreviations are given in Tables 1 and 2, respectively. As shown in a flow resistance study, ovoid forms on a surface have a drag reduction effect.[12] In this study, we focus on the surface condition of the propeller's blade. Protruding hemispheres are adopted on the PS of the blade. The profile of the propeller is shown in Fig. 1; some hemispheres are located on the PS and the geometric parameters of the hemispheres are consistent. These protruding hemispheres have radius r_b and spacing b_i and are distributed along different circular arcs of a curve-based array on the PS.

3.   Grid Generation and Numerical Initialization

The water around the propeller is separated into two domains, a static outer domain and an inner rotating domain, as shown in Fig. 2. The diameter of the rotating domain is 1.2 times the propeller diameter D, and the length of the rotating domain is four times the propeller hub length

Table 1
Geometric parameters and some values.[6]

Parameter	Description	Value
D	Diameter of propeller	250 mm
L	Length of hub	160 mm
n	Rotating speed	1500 rpm
P/D	Pitch ratio	1.02
ε	Rake angle	10 degrees
d/D	Hub ratio	0.18
A_e/A_o	Area ratio	0.65
J	Advance coefficient of propeller	0.1–1.0 in intervals of 0.1
r_b	Radius of protruding hemispheres	0.2, 0.3 mm
b_i	Distance between two adjacent balls	$b_1 = 5$ mm, $b_2 = 12.5$ mm
ρ	Density of water	1000 kg/m^3
μ	Coefficient of dynamic viscosity of water	1.01×10^{-3} Pa·s
r	Offset radius of blade sections	

Table 2
Some abbreviations.

| Parameter	Description	Parameter	Description
V	Speed of advance (m/s)	PS	Pressure surface
R_a	Surface roughness (μm)	SS	Suction surface
T	Thrust of propeller (N)	η	Propeller efficiency in open water
Q	Torque of propeller (N·m)	K_T	Thrust coefficient of propeller
R_ε	Reynolds number	K_Q	Torque coefficient of propeller
rpm	Revolution per minute	Y+	Non-dimensional wall distance
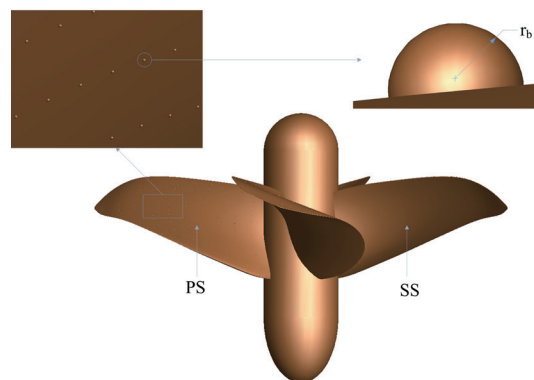
Fig. 1.   (Color online) Propeller and its protrusions on PS.

L. The diameter of the static domain is $5D$ and the length of the static domain is $20L$. All sections have the same centerline.

During hydrodynamic analysis, the distance from the first mesh element to the rotating surface is very important to ensure accurate numerical simulation. If the Y+ value is less than 5, the variation in the CFD difference can be maintained within an acceptable level.[13] All the flow domains are modeled by tetrahedra in ANSYS meshing, and these rotating surfaces have layered inflation, as shown in Fig. 3. In this way, we achieve a Y+ value of the rotating surfaces of less than 5, as shown in Fig. 4.
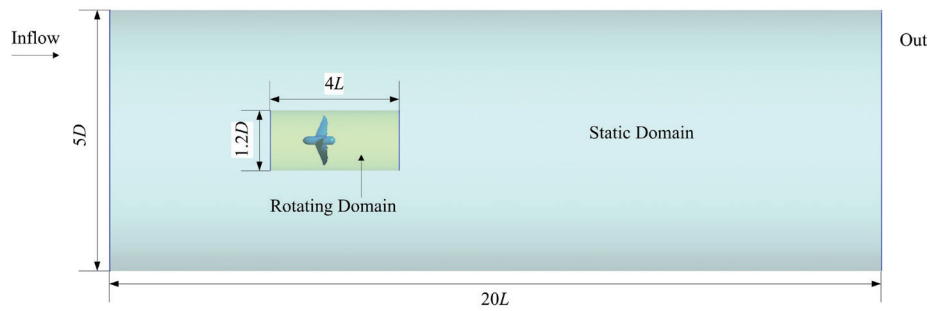
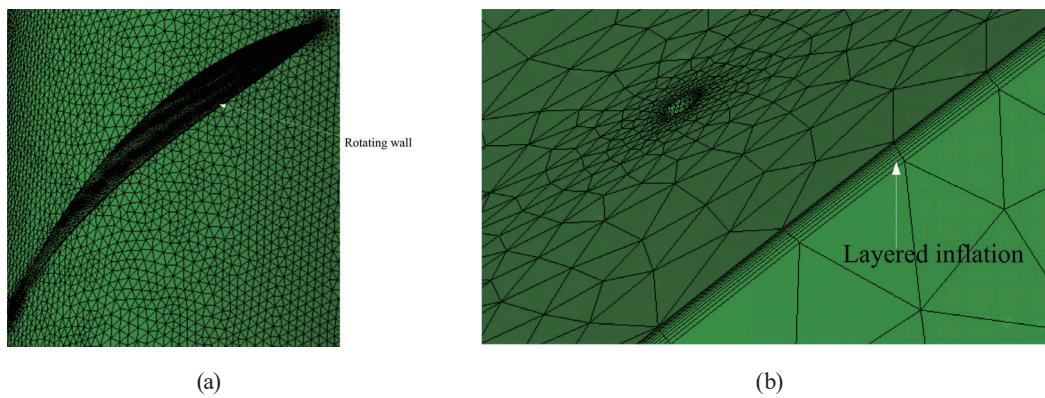Fig. 2.   (Color online) Separate domains during computation.

(a)   (b)

Fig. 3.   (Color online) Grid distribution with layered inflation of rotating surfaces. (a) Rotating wall. (b) Layered mesh.
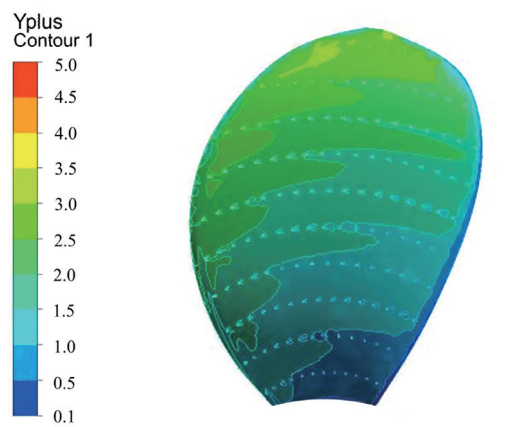

Fig. 4.   (Color online) Y+ distribution on propeller blade with protrusions of $r_b = 0.2$ mm.

In addition to the above meshing, the interface between the rotating domain and the static domain is solved by a frozen rotor mixing model, and the generalized grid interface (GGI) mesh connection method is used to transmit the intersecting hydrodynamic data. The rotating speed is 1500 rpm. The water flows into the static domain with a uniform speed of advance (V). The

relationship between V and J is shown in Eq. (1). The parameters K_T, K_Q, and R_ε are computed using Eqs. (2)–(4), respectively. Then, the efficiency of the propeller η is obtained using Eq. (5).

$$J = \frac{30V}{\pi n D} \tag{1}$$

$$K_T = \frac{T}{\rho n^2 D^2} \tag{2}$$

$$K_Q = \frac{Q}{\rho n^2 D^5} \tag{3}$$

$$R_\varepsilon = \frac{nD^2}{\mu} \tag{4}$$

$$\eta = \frac{J}{2\pi} \cdot \frac{K_T}{K_Q} \tag{5}$$

4.   Performance Results

As expressed by Eq. (4), the Reynolds number R_ε is 9.71×10^3 in this CFD analysis, indicating a turbulent condition. Considering the turbulence and the effect of surface protrusions and roughness on the hydrodynamics, we perform CFD modeling based on the Reynolds-averaged Navier–Stokes (RANS) and averaged continuity equations as follows:[14]

$$\frac{\partial}{\partial x_j}\left(\rho \overline{u_i u_j} + \rho \overline{u_i' u_j'}\right) = -\frac{\partial \overline{p}}{\partial x_i} + \frac{\partial \overline{\tau_{ij}}}{\partial x_j}, \tag{6}$$

$$\frac{\partial(\rho \overline{u_i})}{\partial x_i} = 0, \tag{7}$$

$$\overline{\tau_{ij}} = \mu\left(\frac{\partial \overline{u_i}}{\partial x_j} + \frac{\partial \overline{u_j}}{\partial x_i}\right), \tag{8}$$

where $\overline{u_i}$ is the averaged velocity vector, $\rho\overline{u'_i u'_j}$ is the Reynolds stress tensor, $\overline{p}$ is the mean pressure, $\overline{\tau_{ij}}$ is the mean viscous stress tensor, and μ is the dynamic viscosity.

All the above flow equations are closed using the k-ω SST turbulence model. The hydrodynamic field is calculated through ANSYS CFX commercial software. The inflowing water for different advance coefficients J is set in a steady state. The water is a continuous fluid, and the viscous term is included in the total energy fluid model. The default automatic wall function is used in accordance with the SST turbulence model. All the equations of the turbulence model are solved using a high-resolution scheme, and a root mean square–type convergence criterion with a target residual of 10^{-6} is used.

The hydrodynamic performances of the four propellers examined in this study are calculated for different values of J and are illustrated in Fig. 5. According to the curves, the surface roughness markedly reduces the propeller performance. Compared with the original propeller with a smooth wall,[6] the efficiency of the propeller with roughness is decreased by 2.51% for J = 0.4, by 6.30% for J = 0.9, and by 10.92% for J = 1.0. This phenomenon is consistent with other studies on the effects of surface roughness and fouling on propeller performance.[3,14,15]

In contrast to the surface roughness, the protruding balls on the PS of the blade increase the propeller performance. The thrust force and torque of the propeller for J = 0.9 are shown in Table 3. It is clearly shown that the thrust force of the propeller with protrusions is slightly larger than that of the original propeller. The relative increase in the thrust force is about 0.50% for r_b = 0.2 mm and 0.80% for r_b = 0.3 mm. When the propeller is covered with the protrusions, the relative decrease in torque is about 2.84% for r_b = 0.2 mm and 1.97% for r_b = 0.3 mm. Thus, the efficiency of the propeller can be increased, and the relative increase in efficiency is about 3.43%
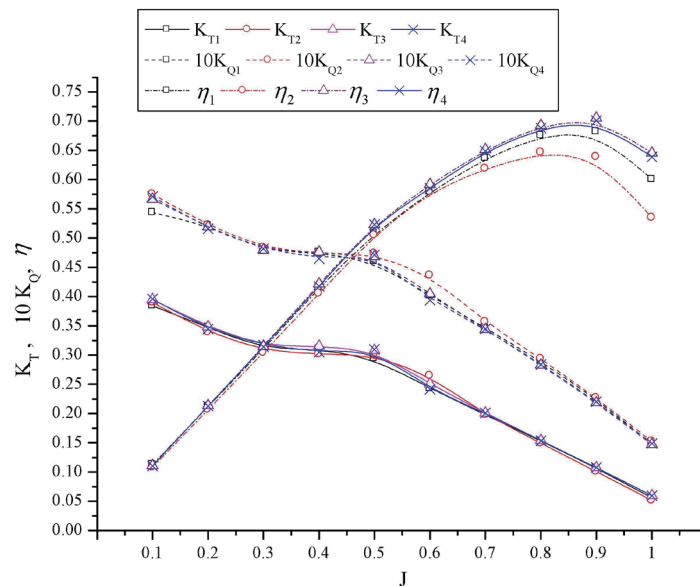

Fig. 5.   (Color online) Performance of different propellers as a function of J. Subscripts 1–4 denote the original propeller with a smooth wall, the original propeller with R_a = 5 μm, the propeller with 0.2 mm protrusions, and the propeller with 0.3 mm protrusions, respectively.

Table 3
Thrust force and torque for $J = 0.9$.

Propeller	Thrust force (N)	Torque (N·m)
Original propeller with smooth wall	261.09	13.72
Original propeller with $R_a = 5$ μm	246.77	13.83
Propeller with $r_b = 0.2$ mm	262.37	13.33
Propeller with $r_b = 0.3$ mm	263.19	13.45

for $r_b = 0.2$ mm and 2.83% for $r_b = 0.3$ mm. Moreover, the relative increase in efficiency increases with the value of J. In contrast, the surface roughness reduces the thrust force and amplifies the torque, thus reducing the efficiency. The trend in efficiency through the variations in the thrust force and torque can be identified using Eq. (5). The protrusions on the propeller PS are beneficial for improving efficiency and reducing energy use.

5.   Discussion

The resistance near a non-smooth surface can be divided into two types. One is the viscous friction resistance based on Prandtl's boundary layer theory. The other is the differential pressure resistance due to pressure changes induced by the fluid at different surface positions. The viscous friction resistance is given by

$$\tau = \tau_v + \tau_y, \tag{9}$$

where τ is the viscous friction resistance, τ_v is the wall shear stress, and τ_y is the Reynolds stress. The protruding hemispheres on the PS are similar to microbumps. Li *et al.* found that when the microbump area ratio is below 0.5, the wall shear stress of the superhydrophobic surface rapidly increases with increasing area ratio of microbumps.[16] In superhydrophobics, the microbump area ratio is the ratio of the surface area of microbumps to the apparent surface area. In this paper, the protrusion area ratio γ is given by

$$\gamma = 4\pi r_b^2 / b_1 b_2, \tag{10}$$

where b_i is the distance between two adjacent balls on the PS.

By referring to Eq. (10), the propellers with protrusions have a γ value that increases with the square of r_b. In this paper, the protrusion area ratio is 0.008 for $r_b = 0.2$ mm and 0.036 for $r_b = 0.3$ mm. The propeller with protrusions of $r_b = 0.3$ mm has a larger shear stress than the propeller with protrusions of $r_b = 0.2$ mm.

Figure 6 shows the wall shear distribution on the PS of each propeller. From the hub to the blade tip, the magnitude of the wall shear stress grows in the outward radial direction. The highest value is at the tip near the leading side. The result for the original propeller with a smooth surface is the same as that reported by Zhu *et al.*[6] The shear stress distribution is almost the same for the propellers with the smooth wall and the surface roughness of $R_a = 5$ μm, but the red area (wall shear > 800 Pa) for the propeller with the rough surface is about three times that for
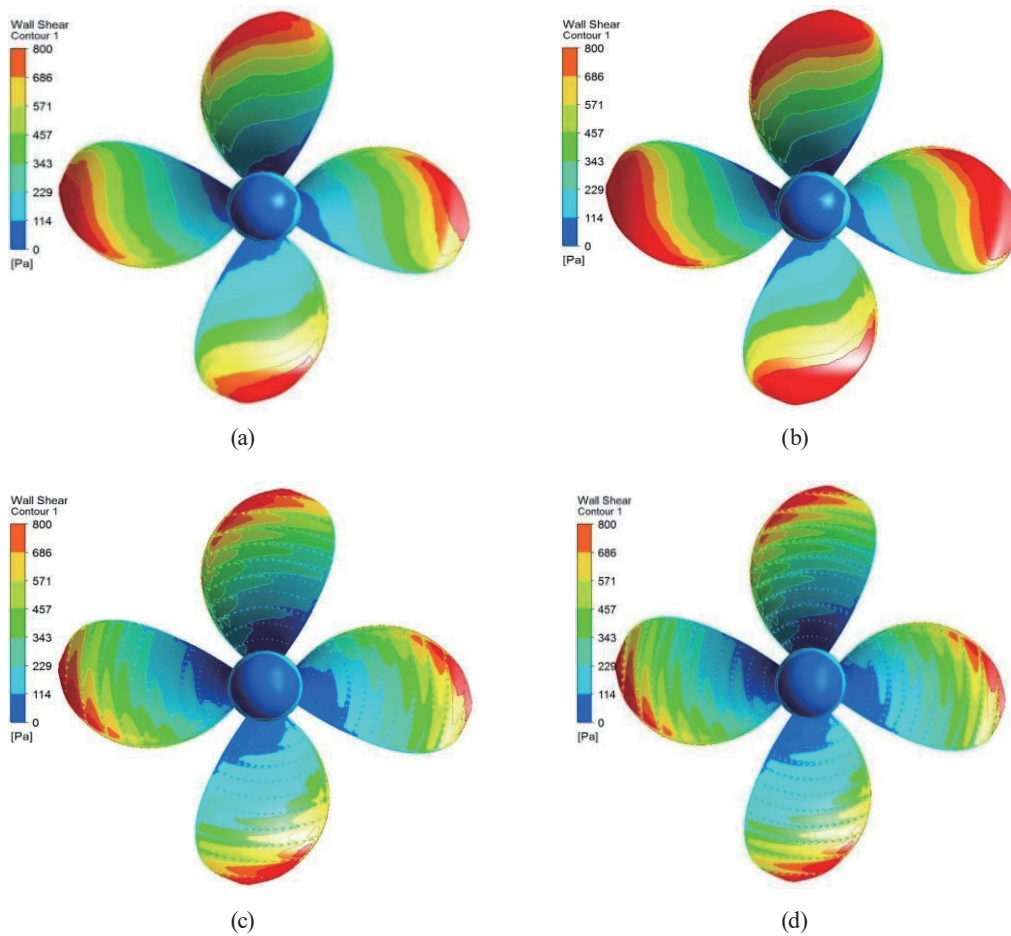
Fig. 6. (Color online) Shear on propeller PS. (a) Original propeller with smooth surface. (b) Original propeller with roughness of $R_a = 5$ μm. (c) Propeller with protrusions of $r_b = 0.2$ mm. (d) Propeller with protrusions of $r_b = 0.3$ mm.

the propeller with the smooth surface. The small protrusions on the PS of the propeller change the flow profile, relieving the wall shear from the leading side to the trailing edge and approximately halving the red area.

Around a rotating propeller, a vortex is always formed by water flowing through the propeller disk. The induced vortex force can reduce the propeller efficiency and have a hydrodynamic impact on shaft detection and sensing systems. Figure 7 shows the turbulence eddy frequency of each propeller. Severe turbulence occurs at the outside and the tip of the blade. The blades with protrusions on the PS have the lowest turbulence eddy frequency. As shown in Fig. 7, before flowing into the propeller disk, the water is in a stable state. However, near the blade surface, there is large turbulence. For example, around the original blade, there is a large layered red area (turbulence frequency > 30000), and there is a hat-like slightly turbulent domain in the wake. For the propellers with surface protrusions in Figs. 7(a) and 7(b), the red layer on the PS is considerably smaller, and the slightly turbulent area on the PS changes to a gentle turbulence layer with waves, where the number of waves (9) is equal to the number of circular arcs in the array of protrusions. Moreover, the turbulent area in the wake is also suppressed to a small cap-like slightly turbulent domain. As shown in Fig. 7(b), the flow turbulence is increased by surface
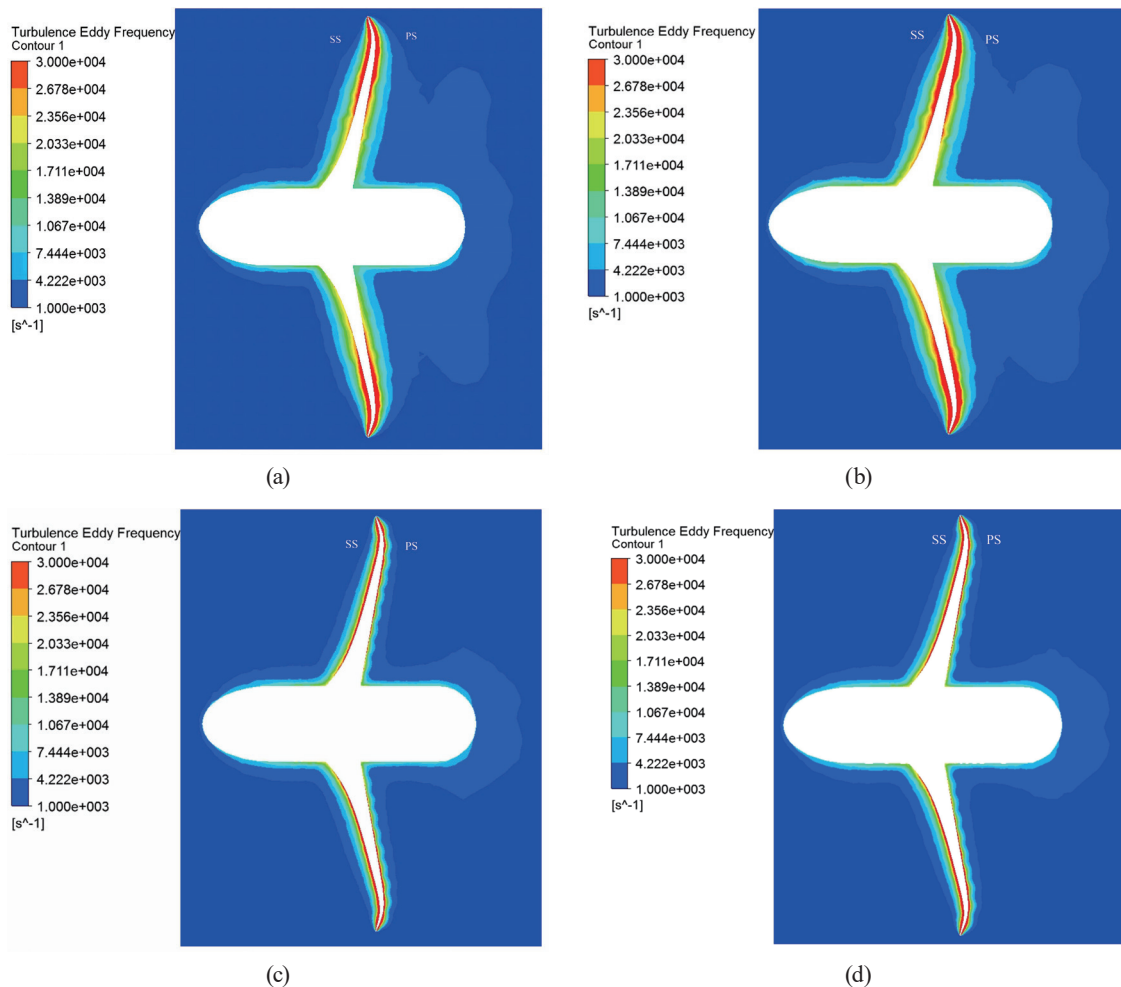
Fig. 7.   (Color online) Turbulence eddy frequency on flow section. (a) Original propeller with smooth surface. (b) Original propeller with roughness of R_a = 5 μm. (c) Propeller with protrusions of r_b = 0.2 mm. (d) Propeller with protrusions of r_b = 0.3 mm.

roughness, and the red band of high turbulence along the blade surface is widened. As shown in Figs. 7(c) and 7(d), there is almost no difference between the two propellers with different sizes of surface protrusions in terms of turbulence.

The pressure distribution on the blade surface is an important determinant of propeller performance, and the pressure is affected by the blade surface profile. Figure 8 shows the pressure distribution around one ball for J = 0.9. The surface pressure is markedly larger on one side of a hemisphere than elsewhere. The surface pressure on the original blade is approximately 1000 Pa, but the surface pressure on the new blade with protruding hemispheres is as high as 10000 Pa. Across these protruding hemispheres, the surface pressure falls to a low value of 1000 Pa, but it increases again on the other side of the hemispheres. The surface pressure around the protrusions increases with their radius r_b.

The pressure distribution on the blade surface of a propeller is crucial to evaluate the cavitation on the blade surface and judge the possibility of critical conditions to improve its
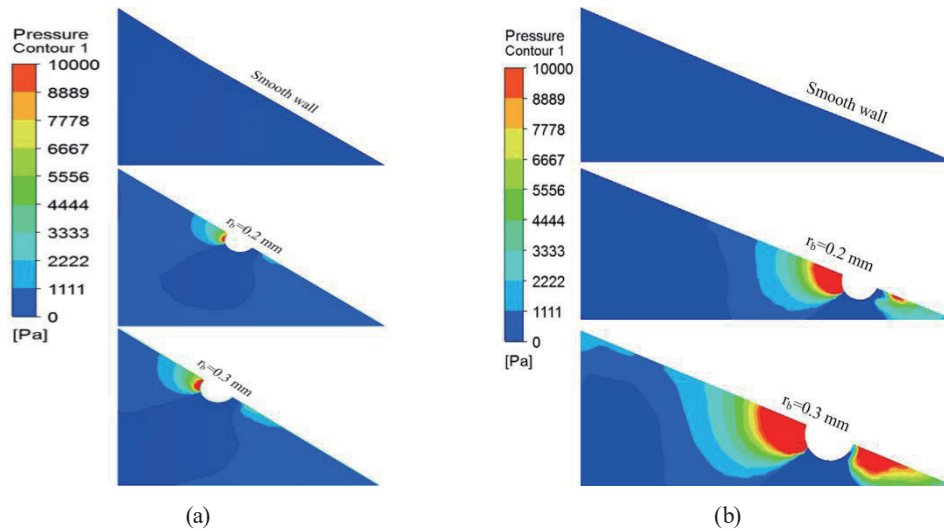
Fig. 8.   (Color online) Pressure distribution around one protrusion on PS at J = 0.9. (a) Blade height 0.4. (b) Blade height 0.8.
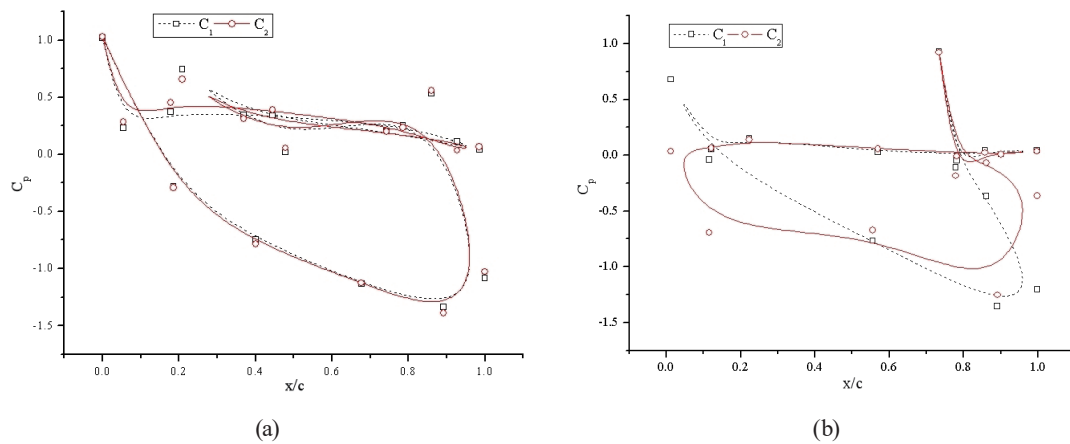

Fig. 9.   (Color online) Distribution of pressure coefficient C_p. C_1, original propeller with smooth surface; C_2, propeller with protrusions. (a) Blade height 0.5. (b) Blade height 0.9.

operation performance. Thus, the surface pressure distribution is used as a reference for propeller design, and C_p is a non-dimensional pressure distribution coefficient defined as follows:[17]

$$C_p = \left(p - p_\infty\right) \big/ \left(0.5\rho U^2\right),$$ (11)

where p is the static pressure on the blade surface, p_∞ is the steady pressure of the inflow, and U is the inflow velocity.

From the above analysis, compared with the original propeller with the smooth surface, there is an obvious difference in C_p on the new propeller with protruding balls of r_b = 0.2 mm. Figure 9 shows the B-spline curves of these two propellers for the pressure coefficient C_p for J = 0.9.

The protrusions increase the pressure along the chord length direction. The positive values of C_p are the same, except at the leading edge, but the negative values of C_p vary largely. The curve shape of the pressure coefficient of the original propeller with a smooth surface is groove-like but that of the new propeller with protrusions is peanut-like.

6. Conclusions

In this study, a propeller with surface protrusions has been designed by hydrodynamics analysis to increase efficiency and improve the suitability of the conditions for monitoring a propeller shaft with sensors. Protruding hemispheres were added to the PS to reduce surface friction. Numerical simulations based on the finite element method were performed in the ANSYS CFX module. The variation and improvement of the propeller performance were compared between four different blade surface conditions.

Compared with the original propeller with the smooth surface, the thrust force is strengthened and the torque is reduced for the propeller with protruding hemispheres on the PS, increasing its efficiency. Moreover, the turbulence around the new propeller is weakened by the surface protrusions, enabling a propeller shaft to be monitored under more suitable conditions, thus protecting the sensors from turbulence and shock. The protruding hemispheres are beneficial for energy saving, as well as for detection and sensing systems used in ship engineering.

Acknowledgments

References

1 Y. Takekoshi, T. Kawamura, H. Yamaguchi, M. Maeda, N. Ishii, K. Kimura, T. Taketani, and A. Fujii: J. Mar. Sci. Technol. **10** (2005) 70. https://doi.org/10.1007/s00773-005-0197-y
2 Z. B. Zeng: Shipbuild. Chin. **59** (2018) 26. https://doi.org/10.3969/j.issn.1000-4882.2018.01.003
3 D. Owen, Y. K. Demirel, E. Oguz, T. Tezdogan, and A. Incecik: Ocean Eng. **159** (2018) 505. https://doi.org/10.1016/j.oceaneng.2018.01.087
4 X. W. Song, P. Z. Lin, R. Liu, and P. Zhou: J. Zhejiang Univ-Sci. A (Appl. Phys. Eng.) **18** (2017) 59. https://doi.org/10.1155/2017/6212605
5 J. G. Mou, D. S. Dai, Y. Q. Gu, J. Liu, S. H. Zheng, and E. Wang: J. Shanghai Jiao Tong Univ. **50** (2016) 306. https://doi.org/10.16183/j.cnki.jsjtu.2016.02.025
6 W. C. Zhu, H. Y. Gao, and Y. C. Song: Proc. ASME 36th Int. Conf. Ocean, Offshore and Arctic Engineering (OMAE, 2017) 62629.
7 C. Z. Han, Y. Long, B. Ji, X. P. Long, and Z. R. Zhang: J. Hydrodyn. **30** (2018) 1186. https://doi.org/10.1007/s42241-018-0127-1
8 S. Kaidi, H. Smaoui, and P. Sergent: J. Hydrodyn. **29** (2017) 154. https://doi.org/10.1016/S1001-6058(16)60727-8
9 Y. M. Yuan, C. Wang, and Z. Ren: J. Harbin Eng. Univ. **40** (2019) 227. https://doi.org/10.11990/jheu.201707063
10 M. Hossein Ghaemi, and H. Zeraatgar: J. Mar. Sci. Technol. **26** (2021) 257. https://doi.org/10.1007/S00773-020-00734-5
11 Z. Zong, Z. C. Hong, H. Zhang, and P. K. Sahoo: J. Mar. Sci. Technol. **23** (2018) 122. https://doi.org/10.1007/s00773-017-0460-z

12 X. W. Song, P. Z. Lin, R. Liu, and P. Zhou: J. Zhejiang Univ-Sci. A (Appl. Phys. Eng.) **18** (2017) 59. https://doi.org/10.1631/jzus.A1500324

13 J. Hu, T. Li, and C. Y. Guo: Ocean Eng. **217** (2020) 107819. https://doi.org/10.1016/J.OCEANENG.2020.107819

14 F. Andrea, D. Nastia, and M. Ivana: Ocean Eng. **219** (2021) 108376. https://doi.org/10.1016/J.OCEANENG.2020.108376

15 K. D. Yigit, T. Osman, and I. Atilla: Appl. Ocean Res. **62** (2017) 100. https://doi.org/10.1016/j.apor.2016.12.003

16 X. L. Li, X. W. Ma, Y. L. Chang, and H. C. Zhang: Surf. Technol. **6** (2017) 42. https://doi.org/10.16490/j.cnki.issn.1001-3660.2017.06.007

17 E. Korkut, M. Atlar, and D. Z. Wang: Int. J. Naval Archit. Ocean Eng. **5** (2013) 81. https://doi.org/10.2478/IJNAOE-2013-0119